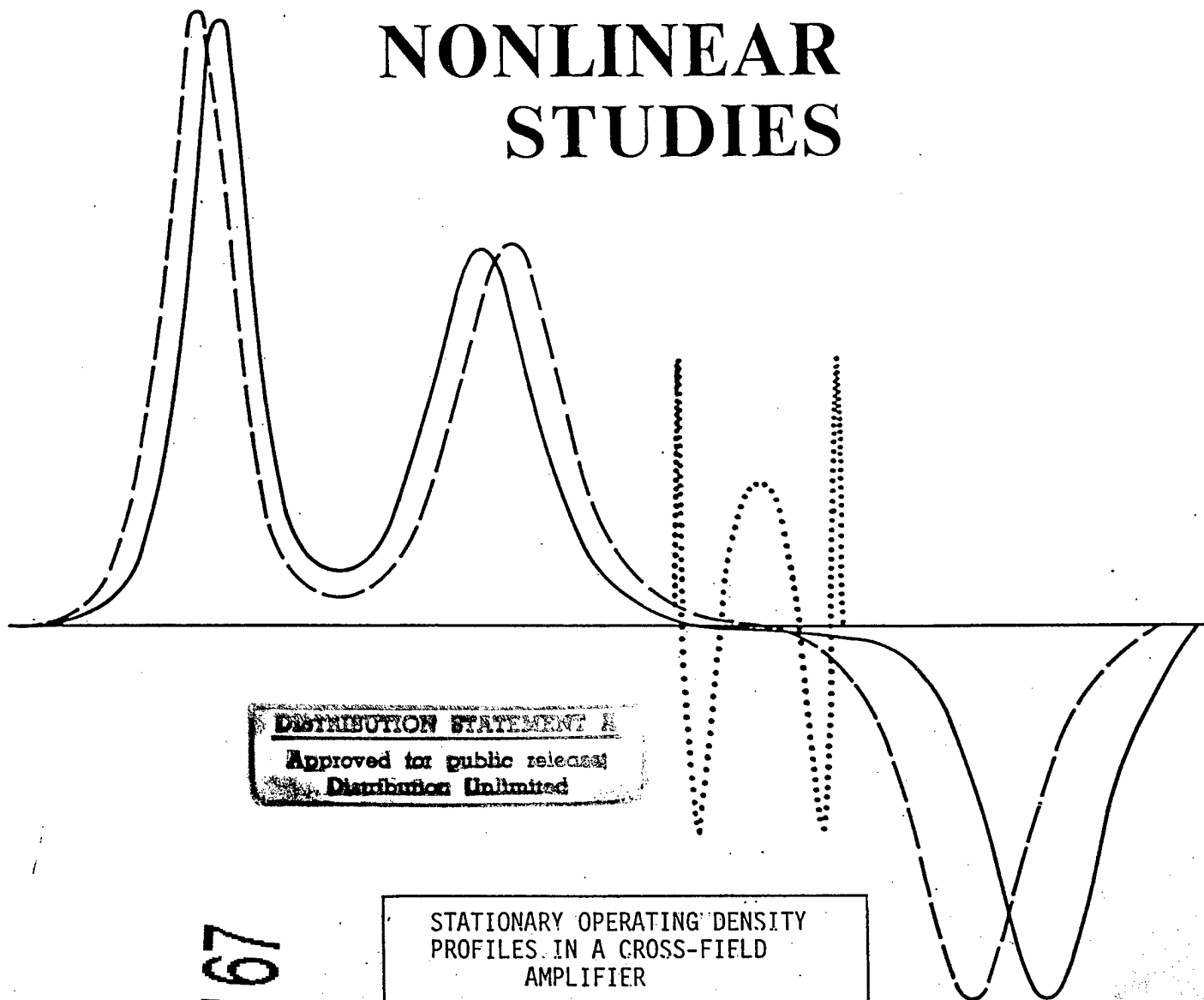


# INSTITUTE FOR NONLINEAR STUDIES



**DISTRIBUTION STATEMENT 1**  
Approved for public release  
Distribution Unlimited

19980422 167

STATIONARY OPERATING DENSITY  
PROFILES IN A CROSS-FIELD  
AMPLIFIER

by

D.J. Kaup  
and  
Gary E. Thomas\*

December 1996

CLARKSON UNIVERSITY  
Potsdam, New York 13699-5815, U.S.A.

\*Communications & Power Industries, 150 Sohler Road  
Beverly, Massachusetts 01915

DTIC QUALITY INSPECTED 3

# STATIONARY OPERATING DENSITY PROFILES IN A CROSSED-FIELD AMPLIFIER

D.J. Kaup<sup>1</sup>

Institute for Nonlinear Studies and Departments of Physics and Mathematics,  
Clarkson University, Potsdam, NY 13699-5815

Gary E. Thomas

Communications & Power Industries, 150 Sohler Road, Beverly, Massachusetts  
01915

## ABSTRACT

We demonstrate with numerical WKB solutions that stationary density profiles can exist in a crossed-field amplifier. These are density profiles that can exist in equilibrium with a high frequency (RF) wave propagating in the slow wave structure. These density profiles are very different from the usual Brillouin profiles. They have a finite and negative density gradient, and extend from the cathode to the anode. They carry a DC current proportional to the RF power in the slow wave structure. The source of the DC current is a wave-particle resonance which occurs toward the top of the sheath. This resonance drives any Brillouin electron flow unstable. The electrons then redistribute themselves into a new flow, one which can be stationary in the presence of the wave-particle resonance. The new flow has a spoke-like structure, where the spokes carry the current to the anode. Various plots are given, including the DC voltage operating range, DC current flow, phase shifts, and density profiles of the total electron distribution, for various ambient magnetic fields and DC voltages. Numerical values agree reasonably well with the modeled experimental device.

PACS numbers: 52.25.Wz; 85.10.Jz; 52.35.Fp

---

<sup>1</sup>the author to whom the correspondence should be addressed; email kaup@sun.mcs.clarkson.edu

# I INTRODUCTION

One of the major problems in the theory of crossed-field devices is to devise methods for determining the operating parameters of an operating device. From numerical simulation with PIC codes, one can obtain estimates of these values [1, 2, 3], but at a very high cost in computational time. Guiding center theory has been used [4, 5] (and references therein) to develop a nonlinear model, in which there is a separation of particle motion into hub motion and spoke motion, as is seen in the numerical simulations. However, this requires a patching of the motion across the hub and the spokes, and also such a theory naturally will require auxiliary parameters, which must be determined. Furthermore, such a model, being based on observations of numerical simulations, tends to lie relatively removed from the basic cold-fluid equations.

In this paper, we report on our results of using a different approach, whereby we decompose the cold-fluid equations into Fourier components, and study the asymptotic solutions of each of the two dominate Fourier components. The purpose of this study is to determine how well one can describe device characteristics with the cold-fluid equations, and also to use this then as a basis for future studies of the noise characteristics of such devices. Here we demonstrate that by simply inputting the characteristic parameters for a given crossed-field device (such as dimensions, dispersion curve for the slow wave structure, operating frequency, ambient magnetic field, etc.), we can predict, reasonably well, the actual operating voltage range of the device vs. the ambient magnetic field, as well as the net phase shift that occurs inside the device and also the operating current density. Furthermore, when we reconstruct the total density from the two main Fourier components, the resulting density profiles are very similar to those seen in numerical simulations. However, our solutions are much smoother, being WKB solutions of the cold-fluid equations and not simulations.

The theory and background of this work has been well detailed in previous works [6, 7]. To summarize those results, the so-called magnetron instability [8, 9] seems to have little to do with the actual operation of crossed-field devices [10]. The instability is indeed there [8], and we do observe effects due to it. However its importance to the operation of a crossed-field device is considerably less than the wave-particle interaction (diocotron). Furthermore, we have been able to show that the classical Brillouin flow [11] in such devices is nonlinearly unstable [6] to the presence of high-frequency (RF) waves propagating in the slow wave structures that these devices contain. The instability initializes as a linear wave-particle instability in a Rayleigh-like equation with a shear flow. Once this linear instability initializes, then it will trigger the nonlinear instability, which is a consequence of second-order (quasilinear) theory [12, 13, 14]. The growth rate of this nonlinear instability is directly proportional to the density gradient at the edge of the sheath [6], which for a Brillouin flow, is very large. The second-order theory then predicts that the electron density will change and evolve. What we find is that it does evolve and it does relax to a new density profile, which is one that will be in equilibrium with the propagating RF wave. This instability of the Brillouin sheath is not surprising since earlier kinetic studies in magnetically insulated diodes [15, 16], had revealed that stochastic electron motion occurs as the Brillouin limit is approached. Thus electrons in a Brillouin flow can be easily perturbed, and kicked out of the flow and into new states.

The physics of this instability is quite simple. One starts with a CFA where the ambient magnetic field is present, the input RF signal is present, and the DC voltage is off and at zero. Presumably, there are a few free electrons present, which by secondary emission, will generate the electron plasma. The input RF signal has a fixed RF frequency,  $\omega$ , and inside the device, it also has a characteristic RF wave vector,  $k$ , which is determined by the dimensions and characteristics of the device and its slow wave structure. One now turns on the DC voltage. However it requires hundreds of oscillations before the DC voltage will reach its final value. As this

voltage slowly increases, secondary emission is generating free electrons and a sheath of electrons, undergoing a classical Brillouin flow is created. At first, this sheath is so thin that no wave-particle interaction with the RF wave in the slow wave structure can occur. While the DC voltage is rising and the device is being filled with plasma, the RF wave vector shifts toward smaller values, since the plasma appears as a conductor to the RF wave. Eventually the sheath becomes sufficiently thick for wave-particle interactions to occur. When this occurs, the electrons at the top of the sheath will have a drift velocity,  $v_d$ , equal to the phase velocity,  $\omega/k$ , of the RF wave. Exactly when this occurs will depend on the value of  $k$ , which does shift as the sheath grows. As the wave-particle interaction turns on, depending on the relative phase of the now seemingly stationary (to the electrons) RF electric field, the initially uniformly distributed electrons can now be bunched and/or accelerated. Some of these electrons will be accelerated, cascading toward the anode. Others will be decelerated, possibly spiraling back into the sheath. In any case, a pattern will develop quite rapidly, with a basic spatial, moving periodicity of  $2\pi/k$ , propagating on an altered background. The problem is therefore to determine this pattern and the altered average background, on which this pattern will propagate.

The relatively slow rise time of the applied DC voltage allows us to approximate this process adiabatically. Due to the rapid nonlinear growth rate of the instability, at any instant, we can consider the applied DC voltage to be a constant, as far as the nonlinear instability is concerned. Thus at each value of the applied DC voltage, we can expect the electron density profile to have responded to the demands of the nonlinear instability, achieving a stationary state [13] for that voltage. These stationary states are, in general, quite different from the classical Brillouin density profiles. In particular, they all have finite, negative density gradients, and they all extend from the cathode to the anode, with a nonzero value of the density at the anode [13]. Furthermore, each state has a nonzero DC current flow where the DC current is proportional to the RF input power. Thus the device acts as an amplifier, delivering power to the RF wave, proportional to the local RF energy density.

Here we shall take the major equations from our previous studies and apply them to a specific tube, calculating the operating density profiles, the operating voltage range, the phase shift per section and the operating current density. The essential equations will be described and discussed in Section II and the numerical results will be presented in Section III. In Section IV, we shall discuss the results of, and defects of the current model, indicating what improvements could be made in the future.

## II BASIC EQUATIONS

The geometry and configuration that we shall be using is shown in Fig. 1, which is a diagram of a "planar magnetron". A planar geometry is preferred for analytical treatment because of its simplicity. Although actual devices are usually cylindrical, the essential physics are contained in the planar model. At the bottom is the cathode, which is an electron emitting material. It is located in the  $xz$ -plane and at  $y = 0$ . We take the ambient magnetic field to be along the negative  $z$ -axis so that the electron drift velocity will be in the positive  $x$ -direction. The electron cyclotron frequency is  $\Omega = eB_0/(mc)$  where  $B_0$  is the ambient magnetic field. Next to the cathode is the electron sheath which extends out for some distance from the cathode. The anode is located at a distance  $\ell$  above the cathode. On the anode is a slow wave structure which is simply a wave guide, along which the RF wave will propagate. This slow wave structure is there to i) slow down the electromagnetic RF wave, which is moving near the speed of light inside the anode structure and ii) to select the effective RF (electrostatic) wave vector,  $k$ , that the plasma will see and will respond to.

The basic cold fluid equations describing this physical system are

$$\partial_t n + \vec{\nabla} \cdot (\vec{v} n) = 0 \quad (1)$$

$$\partial_t \vec{v} + (\vec{v} \cdot \vec{\nabla}) \vec{v} - \vec{\nabla} \phi + \vec{v} \times \vec{\Omega} = 0 \quad (2)$$

$$\nabla^2 \phi = n \quad (3)$$

In the above equations, the fluid velocity vector is in the  $xy$ -plane and all quantities are taken to be independent of the  $z$  coordinate. We have also simplified the notation by taking  $n$  to be the electron plasma frequency squared ( $4\pi e^2 \rho / m$  where  $e(m)$  is the electronic charge (mass) and  $\rho$  is the electron number density) and  $\phi$  to be  $(e/m)$  times the electrostatic potential. We shall use this notation in the remainder of the paper.

These equations, (1)-(3), are then expanded in Fourier components of  $e^{i(kx - \omega t)}$  [13]. On the fast time scale, the DC Fourier component of this expansion gives the “background solution”, which satisfies

$$\vec{v} = v_0(y) \hat{x} \quad (4)$$

$$v_0(y) = \partial_y \phi_0(y) / \Omega \quad (5)$$

where  $\phi_0$  is obtained from Poisson’s equation

$$\partial_y^2 \phi_0 = n_0, \quad \phi_0(0) = 0 = \partial_y \phi_0(0) \quad (6)$$

and where we have taken the background potential,  $\phi_0$ , to be zero at the cathode ( $y = 0$ ) and have imposed the space-charge-limited current condition,  $\partial_y \phi_0(0) = 0$ . Thus from (6), the solution for  $\phi_0(y)$  is determined once  $n_0(y)$  is given. On this fast time scale, the background electron density profile,  $n_0(y)$ , is arbitrary, except that it does have to satisfy one integral condition, and that is that the potential at the anode,  $\phi_0(y = \ell)$ , must equal the applied cathode-anode DC voltage,  $V_0$ . Also, if the background electron density profile is to be linearly stable, then it is necessary for the density profile to always have a non-positive density gradient [12].

Next we consider the fast time scale of the fundamental Fourier components of these equations in the presence of the above background. These can be reduced to [8, 13]:

$$\partial_y p = Au \quad (7)$$

$$\partial_y u = Bp \quad (8)$$

where

$$A = \Omega^2 - \omega_e^2 \quad (9)$$

$$B = \frac{k^2}{A} - \frac{k \partial_y n_0}{\Omega \omega_e A} - \frac{2k^2 n_0 \Delta^2}{\Omega^2 A^2} \quad (10)$$

$$u = -ikv_{1x} \quad (11)$$

$$p = Av_{1y} \quad (12)$$

$$\omega_e = \omega - kv_0 \quad (13)$$

$$\Delta^2 = \Omega^2 - n_0 \quad (14)$$

In the above,  $\omega_e$  is the frequency of the RF wave as seen by the electron moving at the background drift velocity,  $v_0(y)$ , and  $\Delta$  is the local orbital oscillating frequency for

individual particle orbits [17, 18], which would vanish for a Brillouin flow. In (11) and (12),  $v_{1x}$  and  $v_{1y}$  are the  $x$ - and  $y$ -components of the perturbed velocity fields. The perturbed electrostatic potential,  $\phi_1$ , its gradient,  $\partial_y \phi_1$ , and the perturbed electron density,  $n_1$ , are obtained from  $p$  and  $u$  as follows [13].

$$n_1 = ip \left[ \frac{2kn_0^2}{\Omega A^2} - \frac{\partial_y n_0}{A\omega_e} \right] \quad (15)$$

$$\phi_1 = \frac{ip\Delta^2}{Ak\Omega} - \frac{i\omega\omega_e}{k^2} \quad (16)$$

$$\partial_y \phi_1 = \frac{i\Omega}{k}u - \frac{i\omega_e}{A}p \quad (17)$$

The boundary conditions on (7) and (8) follow from the boundary conditions on  $\phi_1$ . At the cathode, which is grounded, the perturbed potential must vanish. Thus  $\phi_1(y=0) = 0$ . Then by (16), one has the ratio of  $u$  to  $p$  at  $y=0$  determined. This determines the solution up to an overall magnitude. One must still match this solution from the cathode-anode region to the solution inside the slow wave structure. In general, this will only occur for selected values of  $k$  and  $\gamma [= \text{Im}(\omega)]$ , which give the possible eigenmodes of these equations. For any eigenmode, it's magnitude can finally be normalized to some fixed value of  $E_{xa}$ , which is the value of  $E_x$  at the vane tips of the slow wave structure.

Next we return to the DC Fourier component and consider the next order slower time scale, which is second order in the amplitude. Once we have a small RF signal oscillating in the device as described above, after many oscillations, due to the nonlinearities in (1)-(3), shifts will start to occur in the background quantities. An analysis of all such shifts was given in Ref. [13], and the results are effectively the same as in the quasilinear theory of Davidson, [12]. The main result is that the background potential (and the background density profile) will evolve according to

$$\partial_\tau \partial_y \phi_0 - \Delta^2 C_2 = D \partial_y n_0 \quad (18)$$

where  $C_2$  is a constant of integration,  $\tau$  is a slow time variable and

$$D = \sum_k \frac{2\gamma p^* p}{\omega_e^* \omega_e A^* A} e^{2\gamma t} \quad (19)$$

which is the quasilinear diffusion coefficient. In (19), the sum is over all modes and  $\gamma$  is the growth rate, which is the imaginary part of the RF frequency,  $\omega$ . Furthermore, this is the asymptotic value of  $D$ , in the limit that  $\gamma t$  is sufficiently large, such that one can ignore the decaying part of the solution. The quasilinear diffusion equation is obtained upon differentiating (18) once. Then from (6) and (14), one finds

$$\partial_\tau n_0 + C_2 \partial_y n_0 = \partial_y (D \partial_y n_0) \quad (20)$$

We now use the adiabatic approximation and impose the condition that  $n_0$  is to be an equilibrium, or stationary density profile, which means that the first term in (20) is taken to vanish. Furthermore, we shall also impose the condition that any electron touching the anode will be immediately absorbed by the anode. Consequently, the density profile would then vanish at the anode. Then upon integrating (20), this gives [6]

$$n_0 = \Omega^2 \left[ 1 - \exp \left[ -C_2 \int_y^l \frac{dy}{D} \right] \right] \quad (21)$$

which defines the steady state equilibrium density profile in terms of the quasilinear diffusion coefficient and the constant  $C_2$ . Given  $D$  and  $C_2$ , this density profile then determines the DC electrostatic potential,  $\Phi_0$ , and therefore the applied DC voltage,  $V_0$ . However, there are no conditions on  $C_2$  and by varying  $C_2$ , one can therefore change  $V_0$ . Conversely, fixing the  $V_0$  will determine a particular value of  $C_2$ . For the stationary states, the significance of  $C_2$  is that it gives the asymptotic DC current density. One may show that the second order DC current density is given by [6]

$$J_{2y} = C_2 \Omega^2 \quad (22)$$

which is a constant, uniform, vertical particle flux.

Thus we now have a means of determining the background DC density profile in an operating device in the adiabatic limit. One wants those density profiles that are in equilibrium with the RF wave propagating in the slow wave structure. The eigenmodes of an RF wave propagating on this density profile could have various different eigenmodes, each of which would satisfy (7) and (8). One would include all these various eigenmodes in the evaluation of the diffusion coefficient by (19). Of all these modes, only the unstable ones need be included, since  $\gamma$  is zero for the stable modes. Furthermore, in the asymptotical limit, since the most unstable mode will dominate, we need to retain only that mode in the sum. Thus we shall take

$$D = \frac{2\gamma p^* p}{\omega_e^* \omega_e A^* A} e^{2\gamma t} \Big|_{\text{most unstable}} \quad (23)$$

Now the problem becomes one of consistency. Can we find a density profile,  $n_0(y)$ , which is stationary, for which, the most unstable RF eigenmode (for the given slow wave structure), generates a diffusion coefficient, which by (21), regenerates the same  $n_0(y)$ ? It turns out that such profiles do exist and they can be determined numerically. Such will be demonstrated in the next section for a particular CFA.

### III NUMERICAL SOLUTIONS

If the stationary density profile is a reasonably stable fixed point of these equations, then we should be able to converge to it from almost any reasonable initial density profile. Thus one should be able to choose some reasonable initial guess for a density profile, calculate the RF eigenvalues for  $k$  and  $\gamma$ , find the most unstable mode, and use that mode to evaluate  $D$  by (23). Now, in order to construct a new density profile from (21), one needs some value for  $C_2$ . This can be determined by choosing values for  $C_2$ , evaluating (21), and integrating twice to find the applied DC voltage,  $V_0$ , for that density profile. Now vary  $C_2$  until the resulting  $V_0$  is the correct value. Once this is accomplished, one then has a new density profile, which should be closer to the desired stationary profile. Now, recalculate the RF fields, recalculate  $D$  and  $C_2$ , and obtain another density profile. Continuing in this manner, we find that the procedure does converge to a stationary density profile.

For numerical simplicity, we shall initially choose a broad, ramped density profile to start with, as shown in Fig. 2, the curve labeled "0". For any density profile,  $n_0(y)$ , and any RF frequency,  $\omega$ , there is usually only one or two unstable eigenmodes of the RF equations, (7) and (8). We will use the modified WKB approximation described in Ref. [6] for the numerical calculations.

To obtain numerical solutions, it is necessary to choose a model for the slow wave structure. The slow wave structure is a wave guide, along which an electromagnetic RF wave can propagate. In the absence of a plasma, it has a dispersion relation,

$\omega_{ct}(k)$ , which defines the modes that can propagate along it. In the presence of a plasma, this dispersion relation will be shifted, depending on how the plasma interacts with the fringe field of the RF wave propagating in the structure. Since we are assuming that the plasma never penetrates into the slow wave structure, we can take the region inside the structure to always be a vacuum region. Therefore inside this region, using Maxwell's equations and taking  $k$  and  $\omega$  to be independent variables, one can solve for the electromagnetic fields inside the structure [19, 20, 21], from which one can determine the fields along the tips of the vanes. In particular, at the tip of the vanes, there will be a definite value for the ratio of the averaged  $x$ - and  $y$ -components of the RF electric field, for any given  $k$  and  $\omega$ . (The overall magnitude of these fields will be determined by the power level of the RF field in the slow wave structure.) This is the value that one must match to the RF plasma solution. Note that we can determine this ratio for the slow wave structure independent of the plasma solution, since the slow wave structure is a vacuum region and thus this ratio will only be a function of  $k$  and  $\omega$ .

The only experimental data available for this particular slow wave structure is the cold-test dispersion curve ( $\omega_{ct}(k)$ ). To extend off of the cold-test curve, and to determine the ratio of the components of the averaged RF fields for other  $k$  values (at the same RF frequency), we shall use a modified comb model, constructed in the following manner. Define  $\rho_{sws}(k, \omega) = -iE_{xa}/E_{ya}$  where  $E_{xa}$  ( $E_{ya}$ ) is the  $x$ - ( $y$ -) component of the RF electric field inside the slow wave structure, evaluated and averaged at the vane tips. The same quantity for the plasma solution will be  $\rho_{plasma} = k\phi_1(\ell)/\partial_y\phi_1(\ell)$  which is the scaled inverse of the logarithmic derivative of the RF electrostatic potential for the plasma solution at the vane tips. For a pure comb model [19, 20, 21], we have  $\rho_{sws}(k, \omega) = f(k)g(\omega)$  where  $f(k)$  is some function of  $k$  and  $g(\omega) = \omega \tan(\frac{s\omega}{c})$ , with  $s$  being the vane depth and  $c$  the speed of light. So, let us take

$$\rho_{sws}(k, \omega) = \frac{g(\omega)}{g(\omega_{ct}(k))} \rho_{sws,ct}(k, \omega) \quad (24)$$

where [19, 20, 21]

$$\rho_{sws,ct}(k, \omega) = \frac{\kappa}{k} \tanh(k\ell) \quad (25)$$

and  $\kappa = \sqrt{k^2 - \omega^2/c^2}$  with the subscripts "ct" indicating the cold test values. Then  $\rho_{sws}(k, \omega)$  will have the correct cold-test limit and otherwise, will behave as a comb model. We shall treat the vane depth,  $s$ , as a free parameter, since if we used the correct value of  $s$ , we would have the wrong value for the  $\pi$ -mode. Rather, we set  $s$  so that the  $\pi$ -mode occurs at the correct frequency. The resulting curves for  $\rho_{sws}(k, \omega)$  for three different frequencies are shown in Fig. 3.

Let us now return to Fig. 2. Here we demonstrate the convergence of our method for finding stationary density profiles. Curve #0 is the initial density profile. We iterate as described above, calculating the RF fields, finding the eigenmode with the largest growth rate, calculating  $D$  from this, using (21) to determine  $C_2$  and the next density profile. As one can see, the profiles are converging to a well defined, stationary, density profile. (This iteration was stopped at iteration #7, for which the change in  $C_2$  and in the eigenvalues,  $k$  and  $\gamma$ , had become less than 1%.) We have found this to be a very general feature of these equations. In all cases so far investigated, where there is at least one unstable mode, this method of solution of the stationary density profiles has been convergent.

Let us now look at a series of such profiles as shown in Fig. 4, where  $V$  is given in units of the cutoff voltage of the ambient magnetic field. Here we have set  $\omega/\Omega = 0.9$  and then varied the DC voltage, looking for possible stationary density profiles. No such solutions seem to exist for  $V \leq 0.60$ . For  $V \geq 0.61$ , we definitely have stationary



density profiles. In the figure, we show that just above threshold, at  $V = 0.65$ , a small ramp structure forms on the Brillouin flow which contains the conducting electrons. As the DC voltage rises, this ramp deforms into a plateau-like structure, with a higher and higher electron density, and at the same time, the current also increases, due to the increased number of electrons available in the region. Finally, at  $V = 0.89$ , the stationary density profile has expanded to occupy almost all the vacuum region. For  $V = 0.90$ , no such stationary density profile seems to exist, in spite of our searching. The conclusion is that the region  $0.62 \leq V \leq 0.89$  is a possible operating regime, and that outside of this region, the tube would not be expected to operate. We shall discuss these points more fully in the last section.

In Figure 5, we expand the above calculations to include several other values of the magnetic field, keeping the RF frequency fixed. Here we present the asymptotic DC current density, as calculate from (22), taking the  $x$ -component of the RF electric field to have a common value for all the DC voltages and ambient magnetic fields. While this condition could be questioned, nevertheless it provides us with a means of commonly comparing the DC currents at different DC voltages and ambient magnetic fields. Here,  $V_r$  is the DC voltage in units of that cutoff voltage where the cyclotron frequency is equal to the RF operating frequency, i.e.  $\Omega = \omega_0$ . When one takes into consideration the surface area of the experimental device, the DC current densities in this figure are comparable with the experimental values. This point will also be further discussed in the Conclusions. For comparison, the experimental analog of Fig. 5 is shown in Fig. 6. Note that the DC voltage and cyclotron frequencies are in the same units as in Fig. 5, however the DC current is in arbitrary units. What one can observe here, is that both curves have the same general trends, but with Fig. 5 containing a wider range of values.

Figure 7 is similar to Figure 5, except that it is for the phase shift per section. Again, these values are in reasonable agreement with the experimental values.

Now, let us go a step further. We have numerical solutions for the background fields (up to second order) as well as for the lowest order of the RF fields. Let us combine these together and see what the total solution would appear to be. In Figure 8, we have composed such a solution for the  $V = 0.65$  solution in Fig. 5, using the same RF amplitude as in Fig. 5. One notes three distinct features. First, there is the characteristic high density, Brillouin flow around the cathode. Second, in the middle of the foreground, there is a weak "spoke" of charge reaching up to and touching the anode. (In the region near the anode, certain parts of the solution were negative. We have replaced those negative values by zeros. We will discuss and justify this approach later.) This is the source of the DC current. Third, one notes that near the cathode, there are relatively large oscillations occurring deep in the sheath where  $v_0$  is very small. These oscillations are due to an almost zero in  $A$ , since  $\omega_e$  is almost equal to  $\Omega$  in that region (the so-called magnetron resonance) [22]. In Fig. 9, we compare the magnitude of  $n_1$  (the Fourier component) with  $n_0$  and plot each as functions of  $y$ . Again, one can see the same three features as in Fig. 8, plus one more, which is the very distinct peak in  $|n_1|$  at the edge of the Brillouin sheath. This is the value of  $y$  at which the wave-particle resonance occurs ( $\omega_e = 0$ ) and this peak shows that a large fraction of the particles at that position are being perturbed.

In drawing Fig. 9, it was necessary for us to normalize the RF amplitude to some value. We choose this normalization factor so that, as is easily seen in Fig. 9, the amplitude of the RF field would be as large as possible, without creating unphysical (negative) density regions. (The total density is  $n_0 + \text{Re}[n_1 * e^{i(kx - \omega t)}]$ , where  $\text{Re}$  indicates the real part. Thus to keep the total density positive for all values of  $x$  and  $t$ , we must maintain  $|n_1| < n_0$ .) This we could easily do for all regions except near the anode. Here, since the boundary condition on  $n_0$  is  $n_0(y = \ell) = 0$ , such is impossible to achieve. However, one must remember that we have, so far, ignored

all the higher harmonics; terms such as  $\text{Re}[n_2^{(2)}(y)e^{2i(kx-\omega t)}]$  in the notation of Ref. [13]. These terms can be expected to be important only in the region near the anode. Consequently, if one did evaluate them and include them in the total density, one can expect their phases to be such, so as to cancel the negative values of the total density. We will return to this point in the Conclusions. But for now, we therefore will allow  $|n_1|$  to exceed  $n_0$  near the anode, and when we calculate the total density by using only the two leading terms, we will replace all negative values with zeros.

In Fig. 10, we show the magnitudes of the Lagrangian displacements for the RF motion of the particles for the  $V = 0.65$  solution in Fig. 5. These displacements are related to  $p$  and  $u$  by [23]

$$\xi_x = in_0\xi_y - \frac{u}{k\omega_e}, \quad \xi_y = i\frac{p}{A\omega_e} \quad (26)$$

As is clear from the figure, at the resonance, there is very large  $x$ -displacement, with the particles undergoing strongly elliptical oscillations, with the  $x$ -displacement even larger than the anode-cathode spacing. However, well above the resonance, in the vacuum region, this motion relaxes to a simple circular cyclotron motion.

In Fig. 11, we show the magnitudes of the RF electrical fields for the  $V = 0.65$  solution in Fig. 5. As one can see, these fields remain essentially zero inside the sheath, where the particles tend to shield them out.

The  $V = 0.65$  solution in Fig. 5 is a solution just above threshold. Let us now consider another solution, one that is well above threshold, has a larger DC current, a larger DC voltage,  $V = 0.70$ , and a larger ambient magnetic field,  $\Omega = 1.25\omega_0$ . In Fig. 12, we show the comparison of the background density with the amplitude of the RF density. In this case, we can take the  $x$ -component of the RF electric field at the anode to be 4 times that of the previous example. Note that the formation of the plateau region has allowed the RF fields to become larger. This represents a 16-fold increase in the local RF power. The total density as a function of  $x$  and  $y$  is shown in Fig. 13. This is similar to Fig. 8, except that now one sees a much larger spoke of charge extending up to the anode. Plots of the Lagrangian displacements and the RF electric field (not shown) are similar to those for the  $V = 0.65$  case, except that the amplitudes are correspondingly larger.

Now let us consider a solution when the ambient magnetic field is much smaller;  $\Omega = 0.833\omega_0$ , and  $V = 0.80$ . Taking the  $x$ -component of the RF electric field at the anode to be 50% larger than in Fig. 5, we have the resulting densities,  $n_0$  and  $|n_1|$ , as shown in Fig. 14. Using this amplitude for the RF fields and combining these values with the proper phases and adding, we obtain Fig. 15. One should note that the magnetron resonance [22] (where  $A = 0$ ) now occurs inside the physical region. However, its amplitude is much smaller than before. The dominate feature is still the wave-particle resonance near  $y = 0.5\ell$ , from which the resulting spoke of charge originates, reaching up to the anode.

## IV CONCLUSIONS

We have shown that the background Brillouin flow in a CFA is significantly changed by presence of an RF wave in the slow wave structure. Starting from a cold configuration, with the ambient magnetic field and the input RF signal present, as the DC voltage is turned on, at first one will have a Brillouin flow. However as the DC voltage is increased, one reaches a DC voltage at which the wave-particle interaction can occur between the electrons at the top of the sheath and the propagating RF wave. At this point, the Brillouin flow becomes unstable [6]. As a consequence of this instability, the background density profile distorts into a new shape, one that is stable and is a

asymptotic, steady state solution. Examples of these asymptotic solutions are given in Fig. 4. The DC current characteristics and the phase shift characteristics of these solutions qualitatively agree with the known experimental characteristics of the CPI #266 tube. What has not been done is to determine how fast this asymptotic state will be reached inside the tube. Until this is done, we cannot make quantitatively comparison with the experimental values for the currents and phase shifts, since we do not know how much of the front of the tube is transversed before reaching these asymptotic states. This is a key problem which needs to be solved.

In spite of that, these results are very encouraging and gives us a qualitatively understanding of some of the important processes that occur inside actual devices, and some quantitative quantities as well. For example, by maximizing the amplitude of  $|n_1|$  subject to  $|n_1| \leq n_0$ , except near the anode, we are able to estimate the maximum power level that can be reached, and thereby could estimate the gain from this theory.

Another problem that needs to be solved in some limit, is the contributions of the higher harmonics to these results. We have already indicated that we would expect them to be important only near the anode, and have used this supposition to justify replacing any negative density values with zeros. So we shall give our reasons here in more detail. First, in general, the harmonics are nonresonant. For any background density profile, it would be an accident if another eigenmode would exist for any harmonic. For the first harmonic, we have  $k = 2k_0$  and  $\omega = 2\omega_0$ , where  $k_0$  and  $\omega_0$  are the RF wave vector and frequency of the input signal. Consequently in general, any harmonic would be a driven solution, determined by the appropriate nonlinear source term. For the first harmonic, this source term would be proportional to the square of the RF field. Looking at Fig. 11, one notes that the RF electric fields are largest at the anode. The same is true for the RF velocities. Thus the square of either of these would extenuate this even more, causing the source terms to become significantly nonzero only near the anode. Of course, the RF density is more slowly varying, so this does not necessarily hold true for all source terms. However, when one also considers that the homogeneous solution of Poisson's equation for the first harmonic would be exponential,  $\sinh(2ky)$ , then these all generally indicate that the harmonic contributions, away from the anode, will generally be small. And until this could be theoretically confirmed, this seems to be a reasonable assumption to use. If this would be the case, then we would only have to appeal to the supposition that the solutions of the full cold-fluid equations will always be physical, in that the density will never go negative. Then considering the nature of the current solutions near the anode, as in Figs. 8, 13 and 15, we would expect the contributions from the harmonics to be generally destructive where the present densities are negative (which are shown as zero in the figures) and to be additive where these densities are positive. The net result of would then be qualitatively the same as given in these figures.

We have assumed the cathode to be a perfect device and to be able to generate electrons on demand. Actual cathodes generate electrons by secondary emission. Some of this could possibly be modeled in the future by modifying our boundary condition at the cathode, which is  $\partial_y \phi_0(0) = 0$ . However, this is still to be explored.

One interesting feature is the existence of the magnetron instability [22],  $A = 0$ , deep inside the sheath. As we have seen in Figs. 8 and 13 for the high magnetic field case, the amplitude of the variations in the particle density can be relatively large, and since it occurs next to the cathode, it may have some important consequences for the emission properties of the cathode [24, 25, 26]. One also notes that in the low magnetic field case, Fig. 15, these oscillations are much smaller. We note that this is also the regime of ultra-low noise, but whether or not these two effects are related,

remains to be seen.

### ACKNOWLEDGMENTS

This research has been supported in part by the Naval Surface Warfare Center, Crane Division and the ONR.

Acknowledgement and Disclaimer: Effort sponsored by the Air Force Office of Scientific Research, Air Force Materials Command, USAF, under contract number F49620-96-C-0031. The US Government is authorized to reproduce and distribute reprints for governmental purposes notwithstanding any copyright notation thereon. The views and conclusions contained herein are those of the authors and should not be interpreted as necessarily representing the official policies or endorsements, either expressed or implied, of the Air Force Office of Scientific Research or the US Government.

### References

- [1] A. Palevski, G. Bekefi, and A. Drobot, J. Appl. Phys. **52**, 4938 (1981).
- [2] G.E. Dombrowski, IEEE Trans. Electron Devices, **35**, 2060 (1988).
- [3] S. Riyopoulos Phys. Rev. E **47**, 2839 (1993).
- [4] R. C. Davidson, Phys. Fluids **27**, 1804 (1984);
- [5] Spillios Riyopoulos, Phys. Plasmas **3**, 1137 (1996).
- [6] D.J. Kaup and Gary E. Thomas, Phys. Plasmas **3**, 771 (1996)
- [7] D.J. Kaup and Gary E. Thomas, *Density Profile and Current Flow in a Crossed-Field Device*, Submitted to J. Plasma Physics.
- [8] O. Buneman, R. H. Levy, and L.M. Linson, J. Appl. Phys. **37**, 3203 (1966).
- [9] T. M. Antonsen, Jr., E. Ott, C. L. Chang, and A. T. Drobot, Phys. Fluids **28**, 2878 (1985).
- [10] Mark K. Jablonski [M. Sc. Thesis, MIT (1992)].
- [11] L. Brillouin, Phys. Rev. **67**, 260 (1945).
- [12] R. C. Davidson, Phys. Fluids **28**, 1937 (1985);
- [13] D. J. Kaup and G. E. Thomas, Stud. Appl. Math **81**, 37 (1989); *ibid.* **83**, 271 (E) (1990).
- [14] R. C. Davidson and K. T. Tang, Phys. Fluids **28**, 1169 (1985).
- [15] M. P. Desjarlais and R. N. Sudan, Phys. Fluids **29**, 1245 (1986).
- [16] M. P. Desjarlais and R. N. Sudan, Phys. Fluids **30**, 1536 (1987).
- [17] D. J. Kaup and G. E. Thomas, Phys. Fluids B **4**, 2640 (1992).

- [18] S. A. Prasad, G. J. Morales, and B. D. Fried, *Phys. Fluids* **30**, 3093 (1987).
- [19] J. C. Slater, *Microwave Electronics* (Van Nostrand, Princeton, NJ, 1959), Chap. 13.
- [20] Ronald C. Davidson, Hei-Wai Chan, Chiping Chen and Steven Lund, *Rev. Mod. Phys.* **63**, 341 (1991).
- [21] Hei-Wai Chan, Chiping Chen and Ronald C. Davidson, *J. Appl. Phys.* **73**, 7053 (1993).
- [22] T.M. Antonsen, Jr., E. Ott, C.L. Chang, and A.T. Drobot, *Phys. Fluids* **28**, 2878 (1985).
- [23] P. G. Drazin and W. H. Reid, *Hydrodynamic Stability*, Ch. 4 [Cambridge University Press, New York, (1981)].
- [24] Y. Y. Lau and D. Chernin, *Phys. Fluids B* **4**, 3473 (1992).
- [25] Y. Y. Lau, P. J. Christenson and D. Cherin, *Phys. Fluids B* **5**, 4486 (1993).
- [26] P. J. Christenson and Y. Y. Lau, *Phys. Plasmas* **1**, 3725 (1994).

## FIGURE CAPTIONS

Fig. 1: The geometry and configuration of a planar magnetron or CFA. The magnetic field is directed into the paper and the electron drift velocity is to the right. The  $z$ -axis is perpendicular to the paper, the  $x$ -axis is parallel to the cathode surface and the  $y$ -axis is perpendicular to the cathode.

Fig. 2: A demonstration of the convergence to a stationary density profile, normalized to the Brillouin value of  $\Omega^2$ . The DC voltage is 0.70 of the cutoff voltage,  $\ell$  is the anode-cathode spacing, and  $\omega_0/\Omega = 0.90$ , where  $\omega_0$  is the RF frequency used in these calculations. The numbers refer to the iteration number, with zero being the initial ramped density profile. Iteration was continued until  $k$ ,  $\gamma$ , and  $C_2$  changed by no more than 1%. Not all iterations are shown.

Fig. 3: Plots of  $\rho_{\text{sws}}(k, \omega)$  of the modified comb model which was used in these calculations.  $\omega_0$  is the RF frequency used in these calculations, and  $\ell$  is the anode-cathode spacing.

Fig. 4: Stationary density profiles obtained for  $\omega_0/\Omega = 0.9$ , where  $V$  is the applied DC voltage, in units of the cutoff voltage for this cyclotron frequency,  $\Omega$ . At  $V = 0.60$ , the tube is nonconducting and is just below turn-on, which occurs at  $V = 0.62$ . Note the clear Brillouin structure in this limit. At  $V = 0.65$ , a distinct ramp structure forms and the tube becomes conducting. At higher voltages, the current increases and the ramp turns into a relatively high density plateau. At  $V = 0.90$  (not shown), this system does not seem to have a stationary density profile.

Fig. 5: Current density for selected stationary density profiles, for a fixed  $x$ -component of the RF electric field at the vane tips, as a function of the DC voltage,  $V_r$ , and for various values of the magnetic field. Here,  $V_r$  is measured in units of the cutoff voltage for the cyclotron frequency,  $\Omega$ , equal to the RF frequency,  $\omega_0$ . This figure also outlines the possible DC voltage operating regime, as a function of the ambient magnetic field.

Fig. 6: Experimental curves corresponding to Fig. 5. The current is in arbitrary units, but the values of the cyclotron frequency and the DC voltages are in the same units as in Fig. 5. There is a cutoff at the upper range of current, due to a limitation in the current measuring device used.

Fig. 7: Same as Fig. 5, except that it is for the phase shift per section.

Fig. 8: Plot of the asymptotic solution for  $n(x, y)$  vs.  $x$  and  $y$  for one period of the propagating RF wave, and for the  $V = 0.65$  solution shown in Fig. 4. The  $x$ -component of the RF electric field at the vane tips is the same as in Fig. 5. Note the structure in the foreground, which is the spoke of charge, reaching the anode and carrying the DC current. The slow oscillation seen near the cathode and deep in the sheath is due to the "magnetron resonance", where  $\omega_e = \Omega$ . However since  $\omega_0 < \Omega$ , the resonance doesn't occur inside the physical region, and one is only seeing a disturbance due its close proximity in phase space.

Fig. 9: Plot of the magnitude of the RF density,  $n_1(y)$ , in comparison to the background density,  $n_0(y)$  for the solution in Fig. 8. Note that this is the largest expected value of the RF density, since a larger value would give a negative (unphysical) density in the region of the resonance, near  $y = 0.38$ . Near the anode, one expects the higher order harmonics to become significant, which would then maintain a positive density in that region. (See the discussion in the Conclusions.)

Fig. 10: Plot of the magnitudes of the RF Lagrangian displacements for the solution in Fig. 8, as a function of  $y$ . Note that at the resonance,  $\xi_x$  becomes very

large, which results in very large horizontal excursions of the electrons. Above the resonance, the particle motion become a simple circular cyclotron motion.

Fig. 11: Plot of the magnitudes of the RF electrical fields for the solution in Fig. 8, as a function of  $y$ . Note that inside the plasma, the particles tend to shield these fields.

Fig. 12: Plot of the magnitude of the RF density,  $n_1(y)$ , in comparison to the background density,  $n_0(y)$  for a higher DC current case;  $V = 0.70$  and  $\Omega/\omega_0 = 1.25$ . Here we can take the RF amplitudes to be 4 times that in Fig. 5.

Fig. 13: Plot of the asymptotic solution for  $n(x, y)$  vs.  $x$  and  $y$  for one period of the propagating RF wave for the solution shown in Fig. 12, where the  $x$ -component of the RF electric field at the vane tips is 4 times that of Fig. 5. Note the structure in the foreground, which is the spoke of charge, which is now much larger. The slow oscillation seen near the cathode and deep in the sheath is again due to the "magnetron resonance", where  $\omega_e = \Omega$ . However since  $\omega_0 < \Omega$  still, the resonance doesn't occur inside the physical region, and one is only seeing a disturbance due its close proximity in phase space.

Fig. 14: Plot of the magnitude of the RF density,  $n_1(y)$ , in comparison to the background density,  $n_0(y)$  for a lower magnetic field case;  $V = 0.80$  and  $\Omega/\omega_0 = 0.833$ . Here we can only take the RF amplitudes to be 50% larger than that in Fig. 5.

Fig. 15: Plot of the asymptotic solution for  $n(x, y)$  vs.  $x$  and  $y$  for one period of the propagating RF wave for the solution shown in Fig. 14, where the  $x$ -component of the RF electric field at the vane tips is 50% larger than that of Fig. 5. Note the structure in the foreground, which is the spoke of charge, which is still much larger. The slow oscillation seen now above the cathode and but still deep in the sheath is again due to the "magnetron resonance", where  $\omega_e = \Omega$ . For this case,  $\omega_0 > \Omega$  and the resonance now occurs inside the physical region. However, its amplitude is much smaller than in the other two cases.

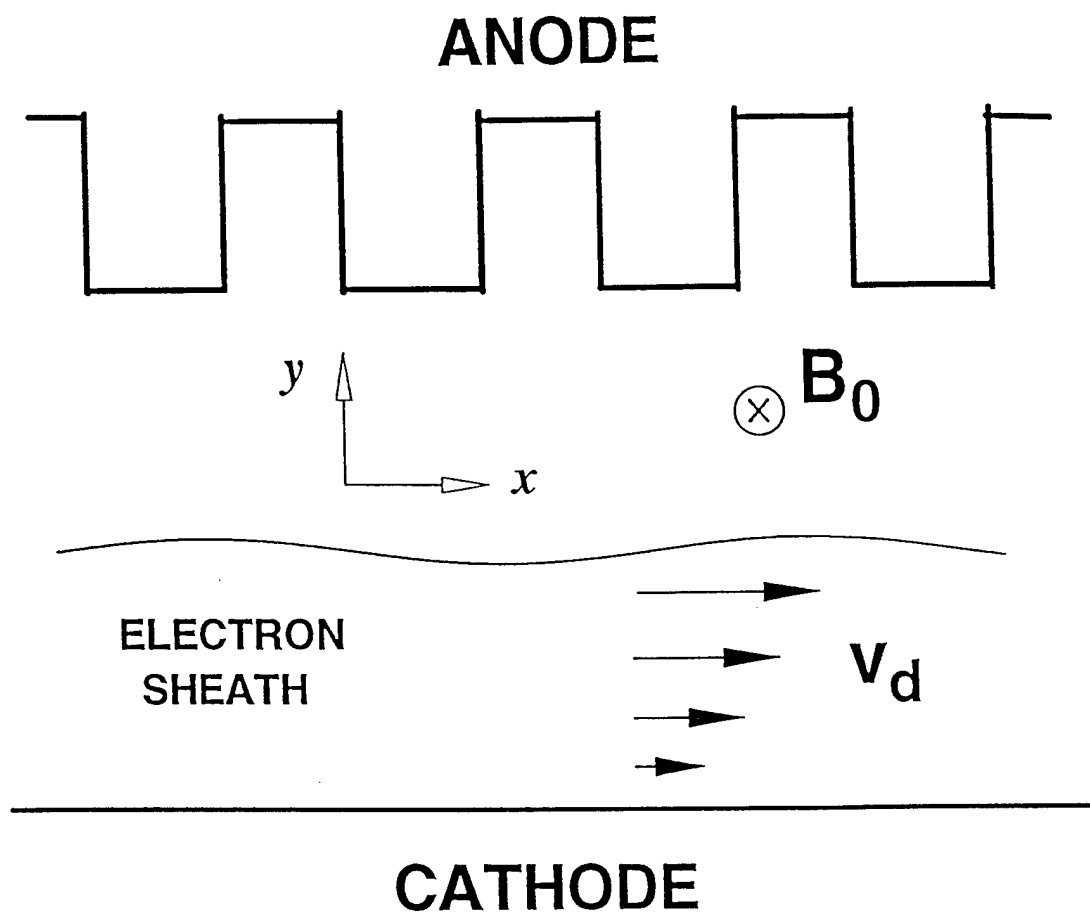


Fig. 1



Fig. 2

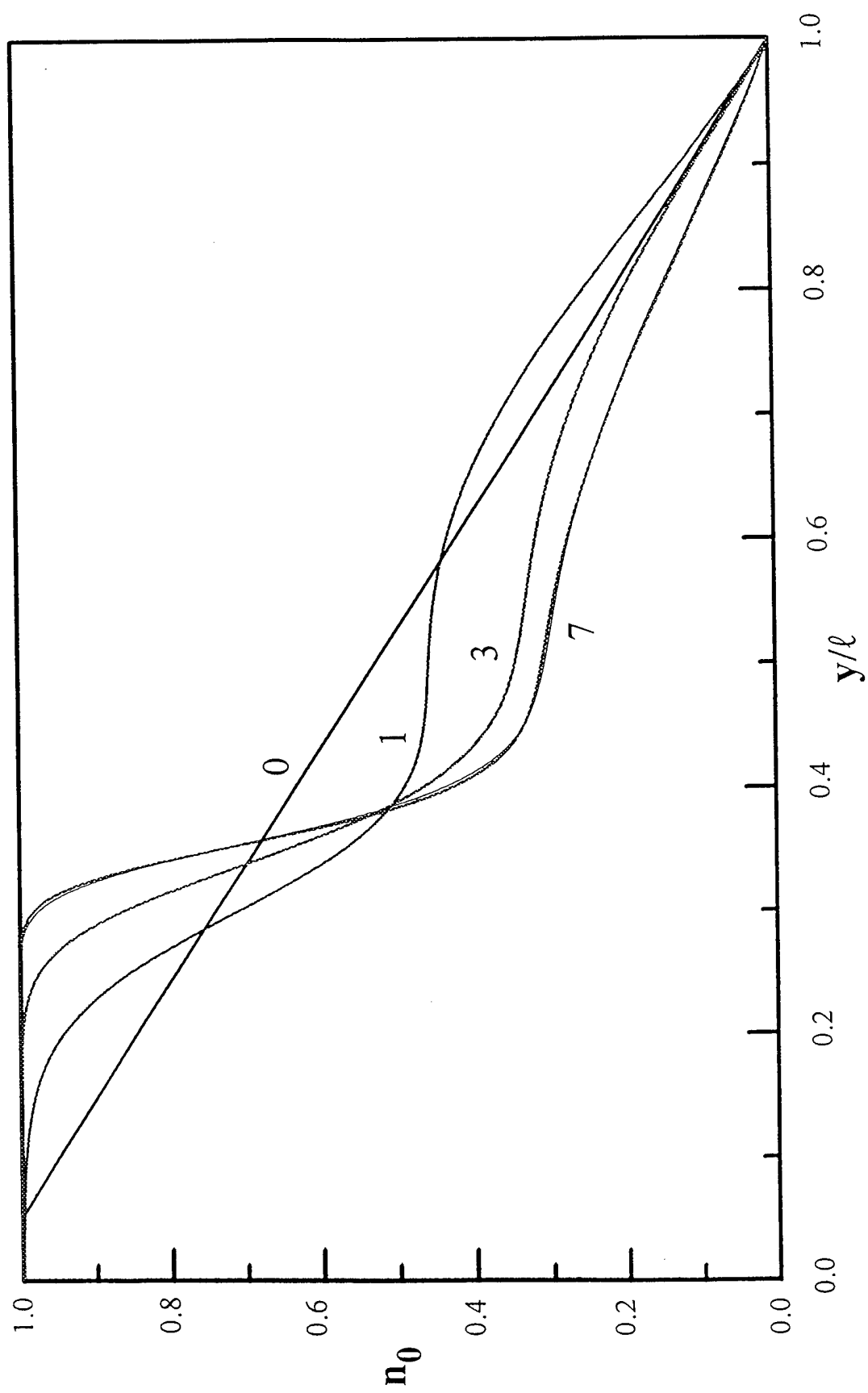
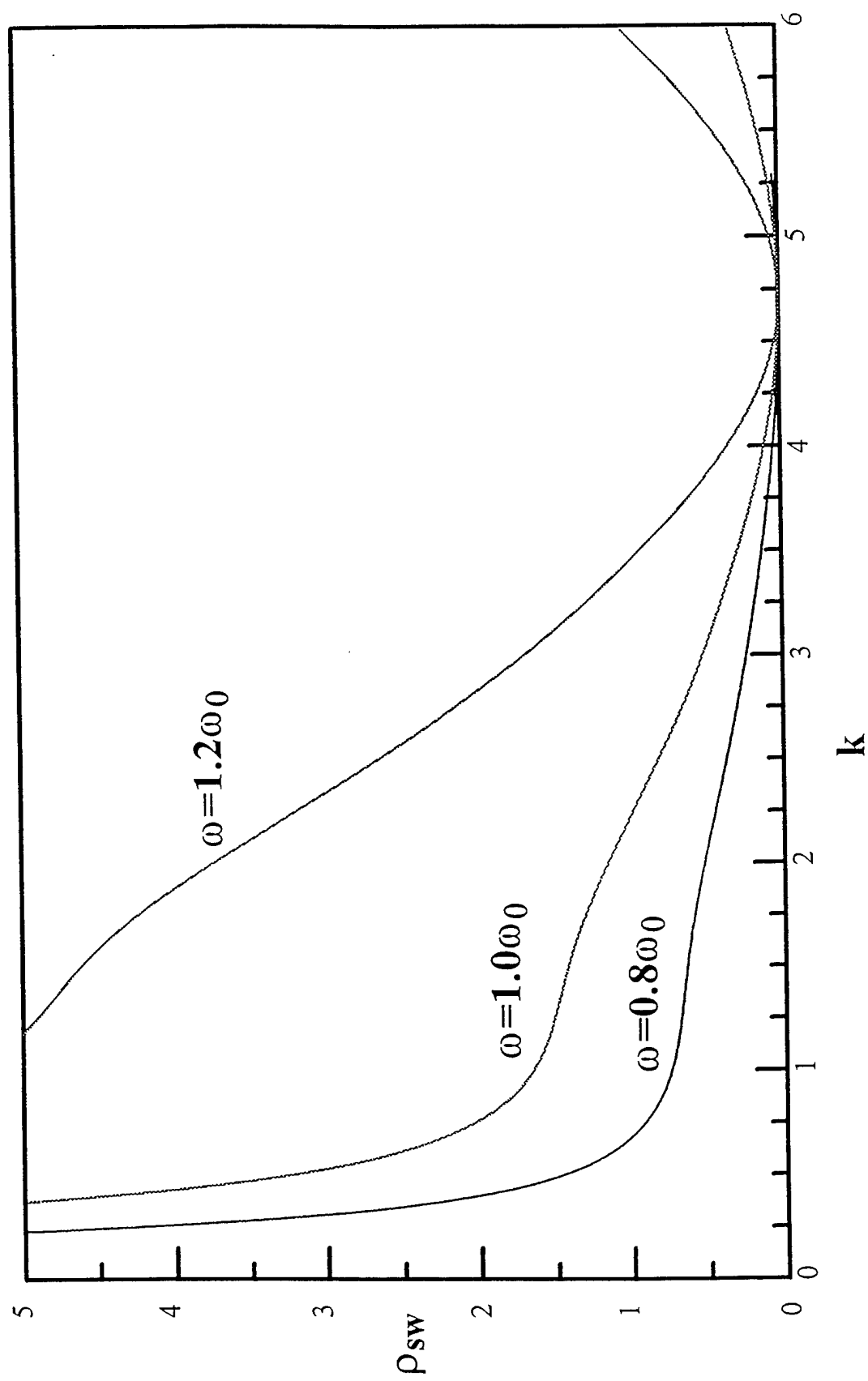


Fig. 3



**Fig. 4**

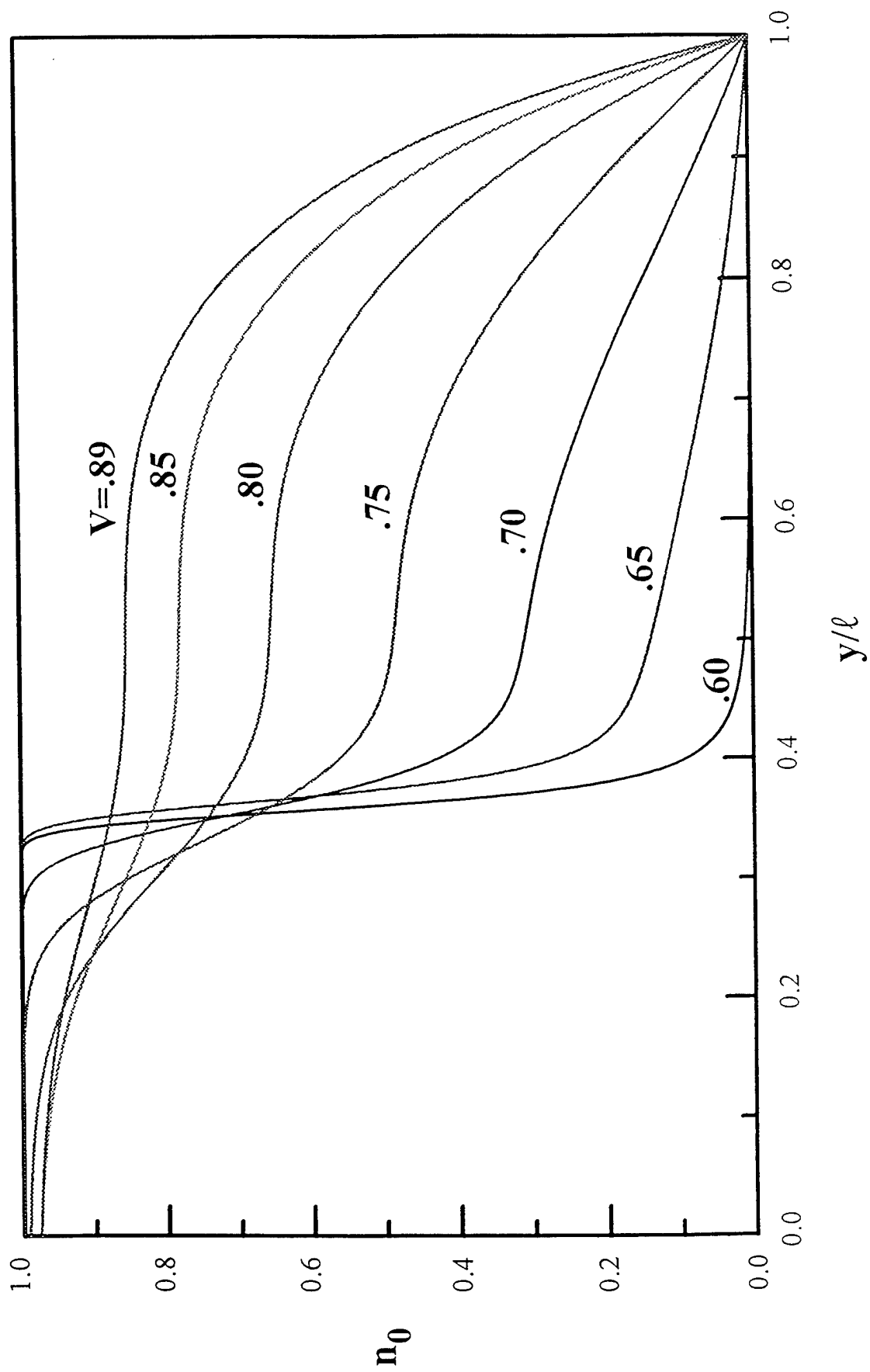


Figure 1 is a plot showing the radial velocity  $V_r$  (Y-axis, ranging from 0.0 to 2.0) versus the dimensionless parameter  $J_y$  (X-axis, ranging from 0.0 to 1.0). The plot displays several curves corresponding to different values of the ratio  $\Omega/\omega_0$ , labeled as 1.54, 1.43, 1.33, 1.25, 1.11, 0.95, 0.83, and  $\Omega/\omega_0 = 0.71$ . The curves generally show that  $V_r$  decreases as  $J_y$  increases, with the rate of decrease being more pronounced for higher values of  $\Omega/\omega_0$ .

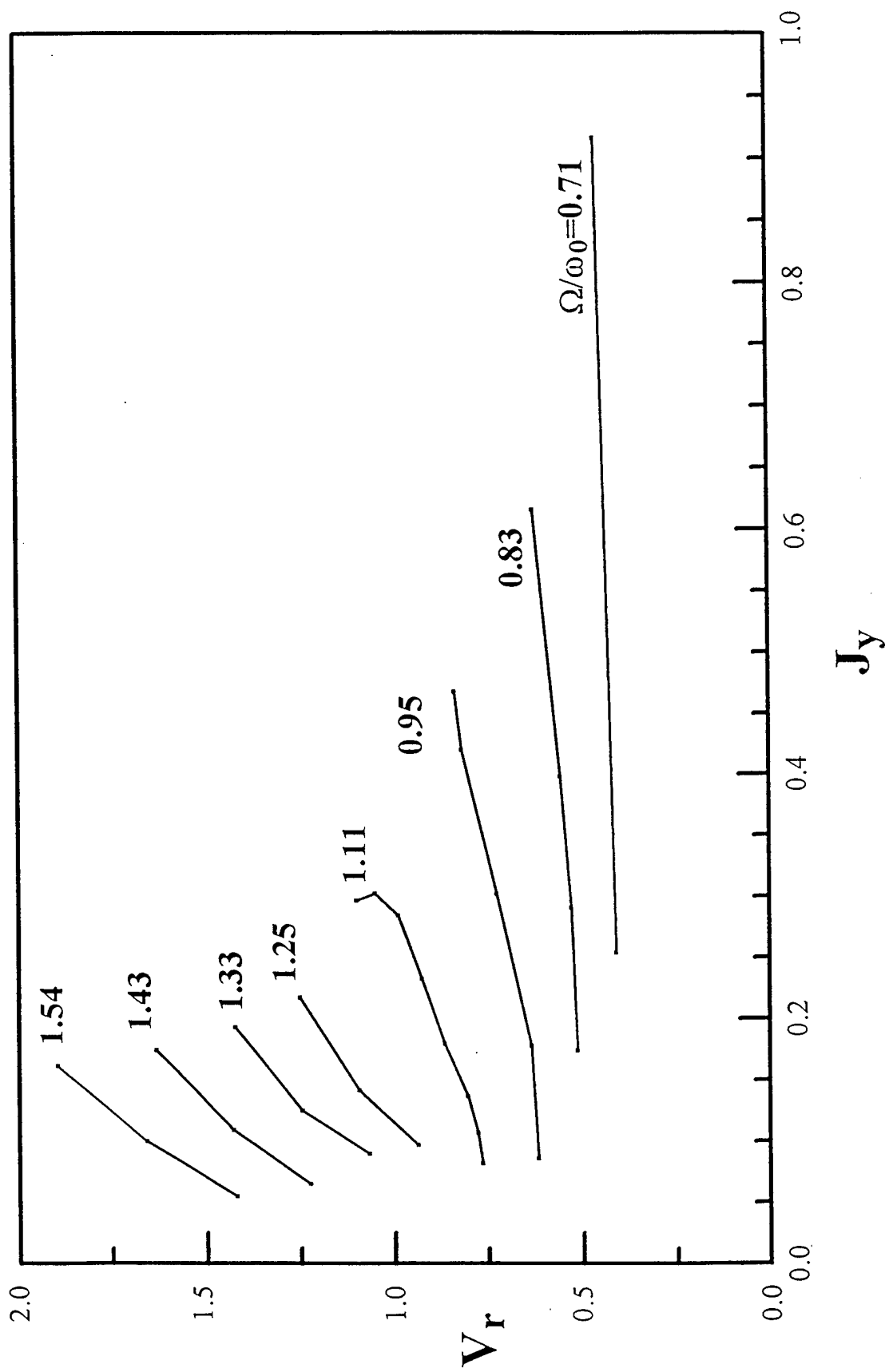


Fig. 6

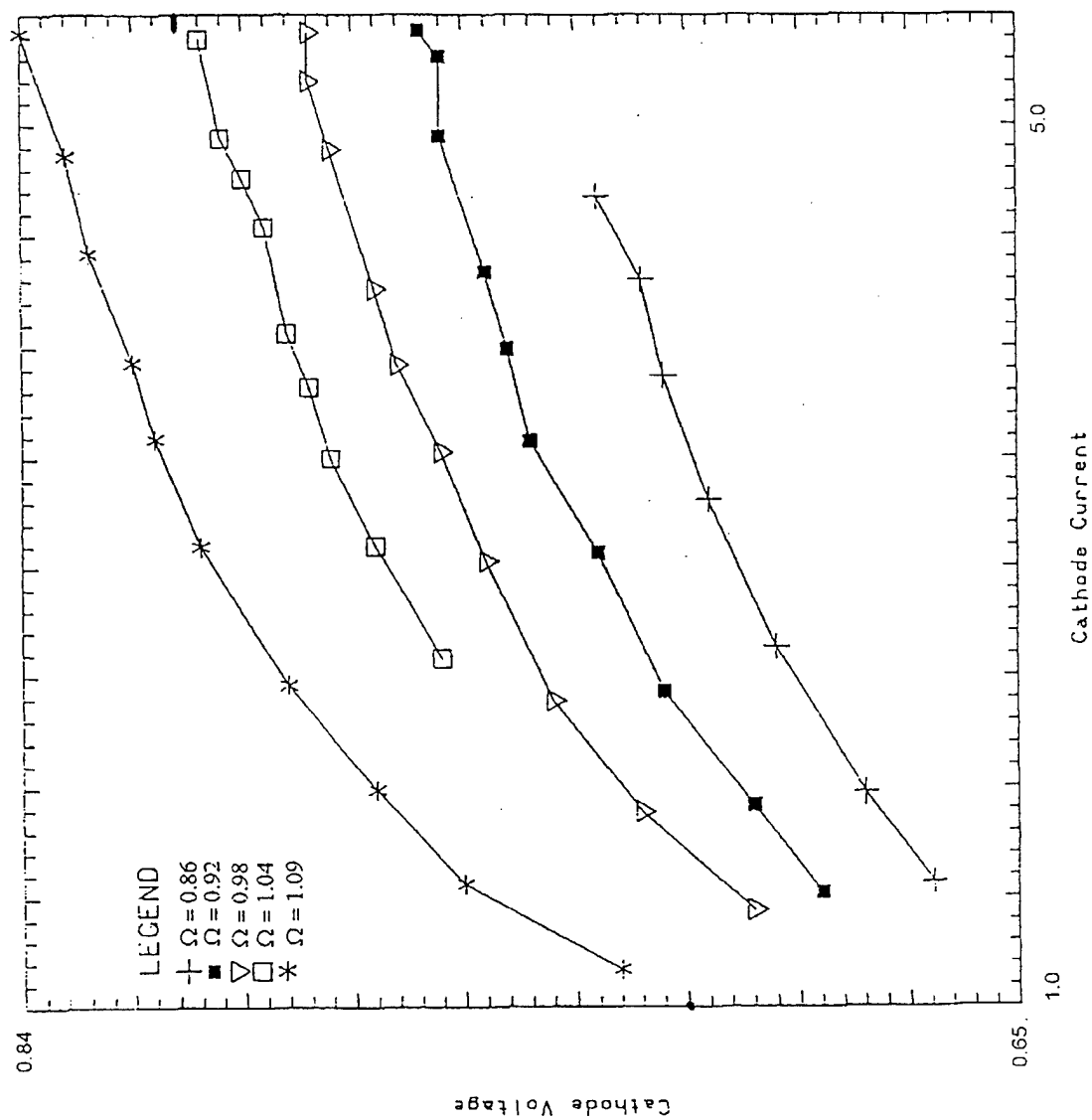


FIG. 7

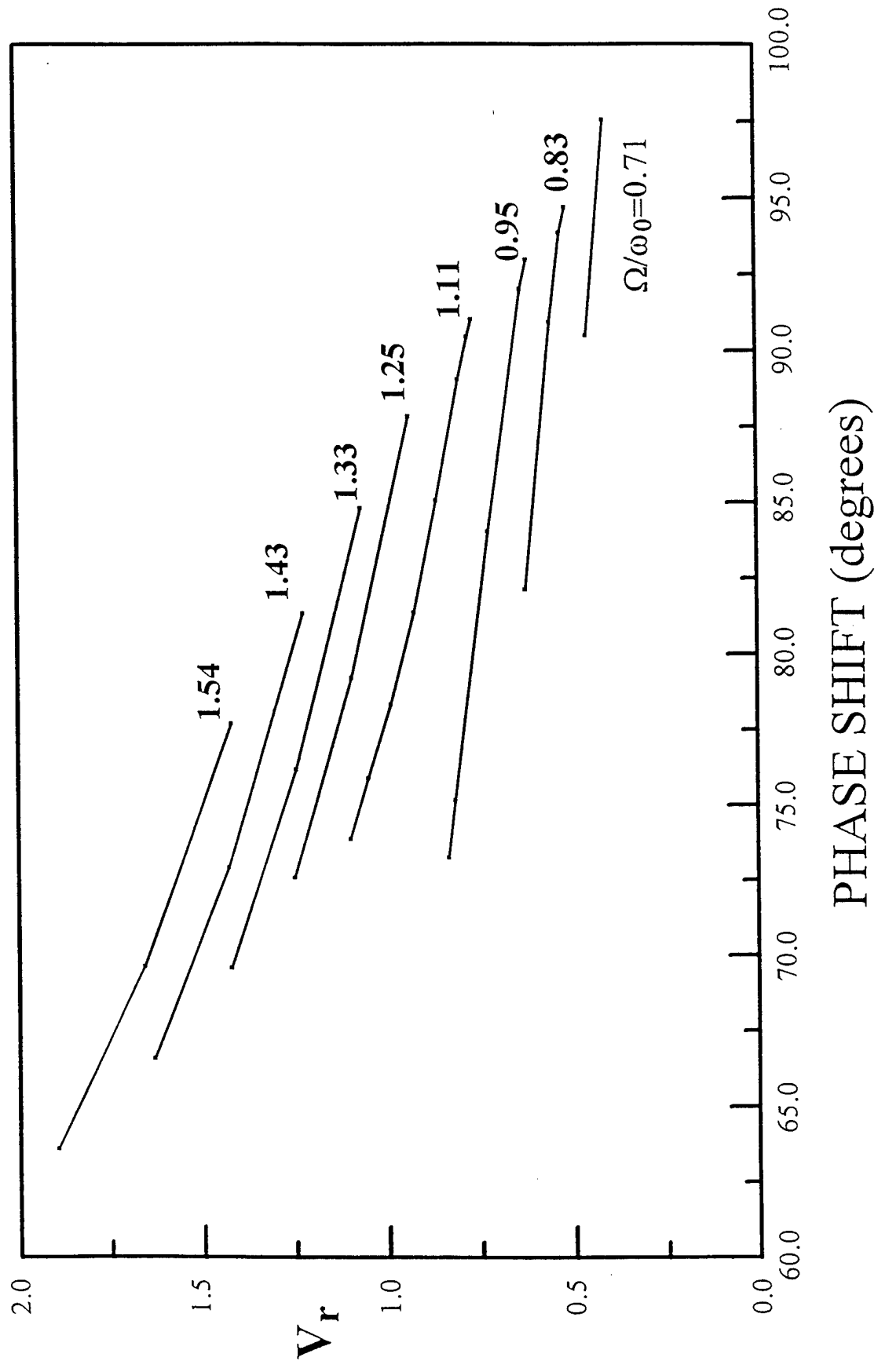


Fig. 8

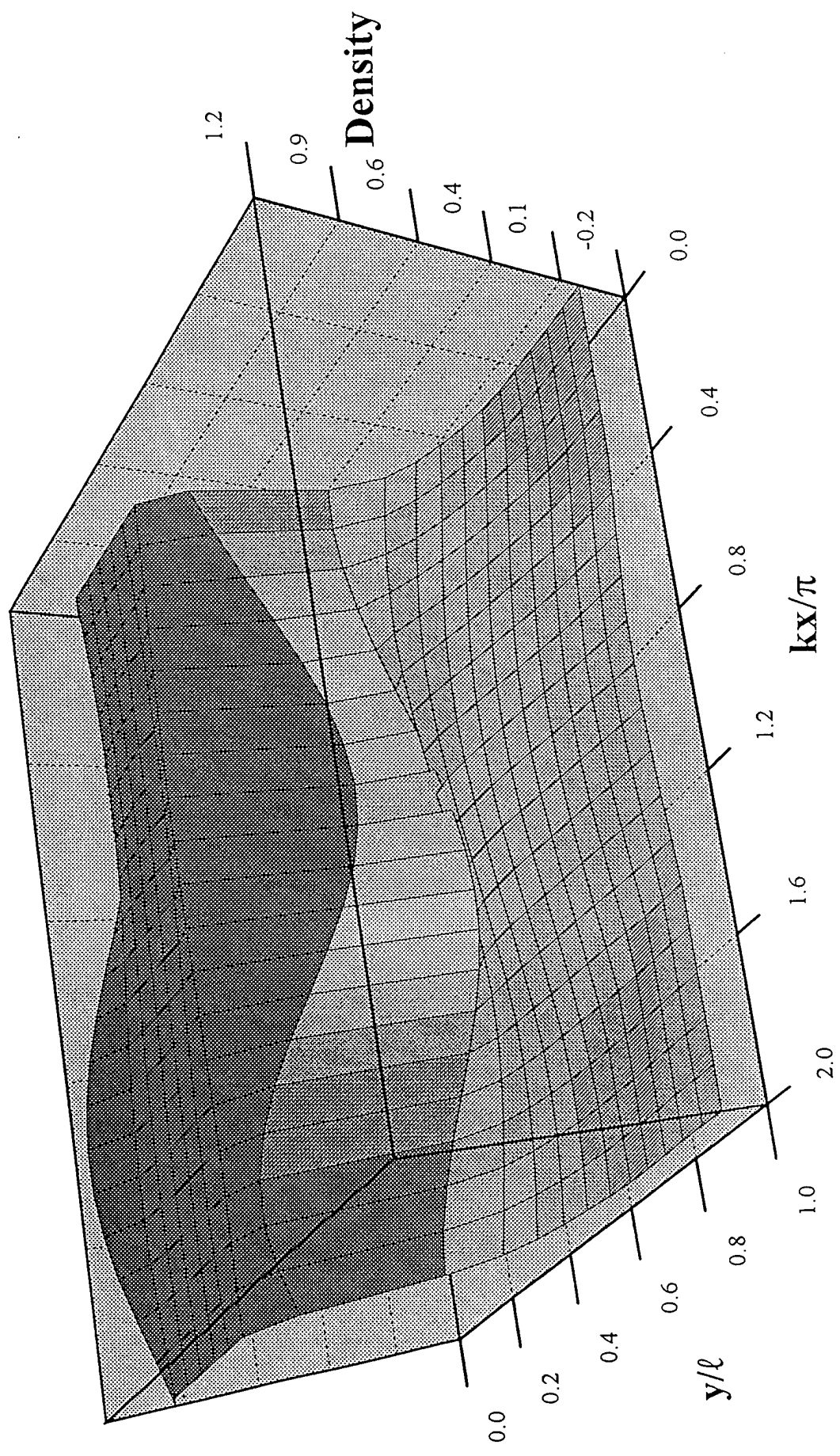


Fig. 9

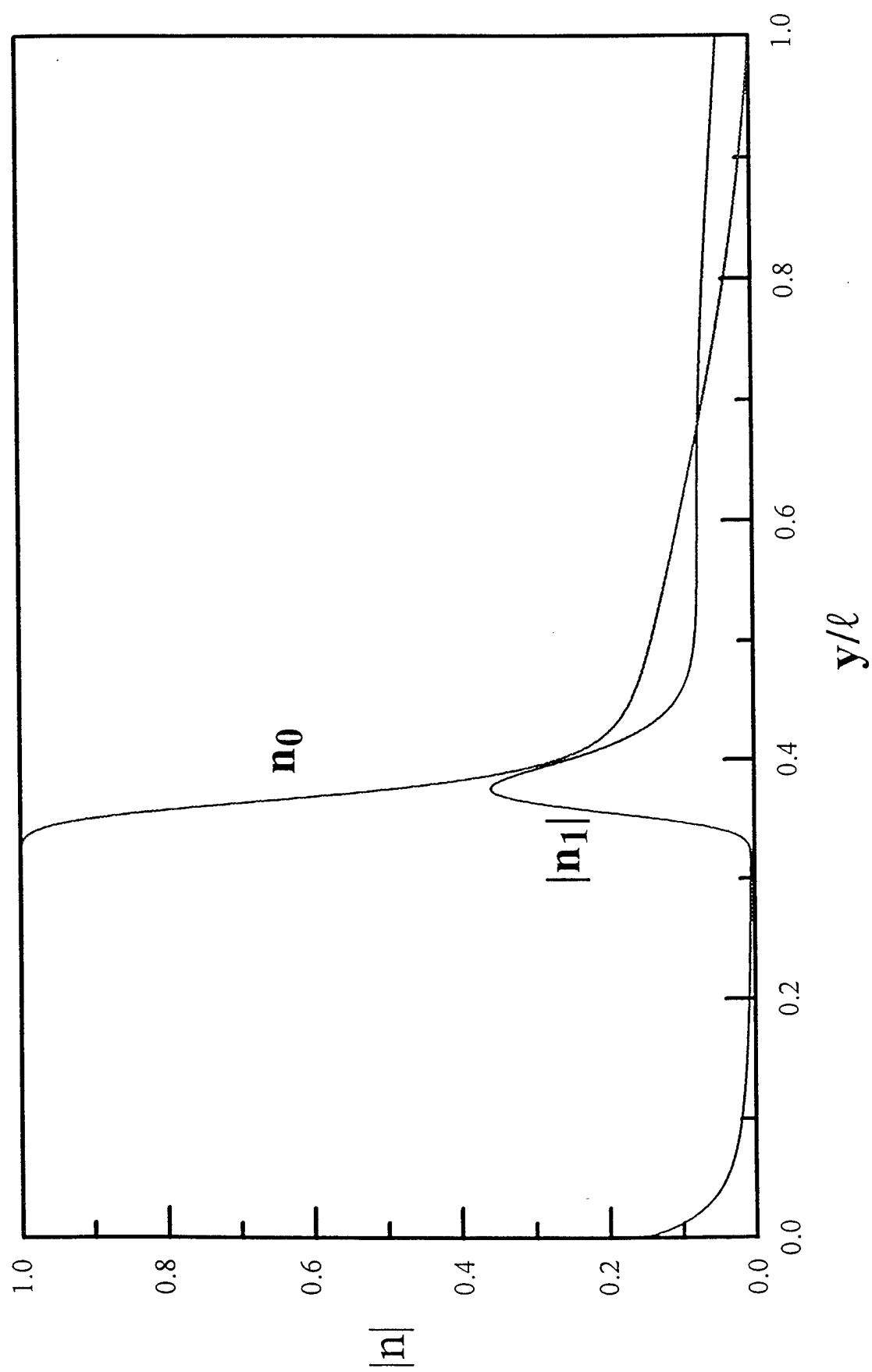




Fig. 10

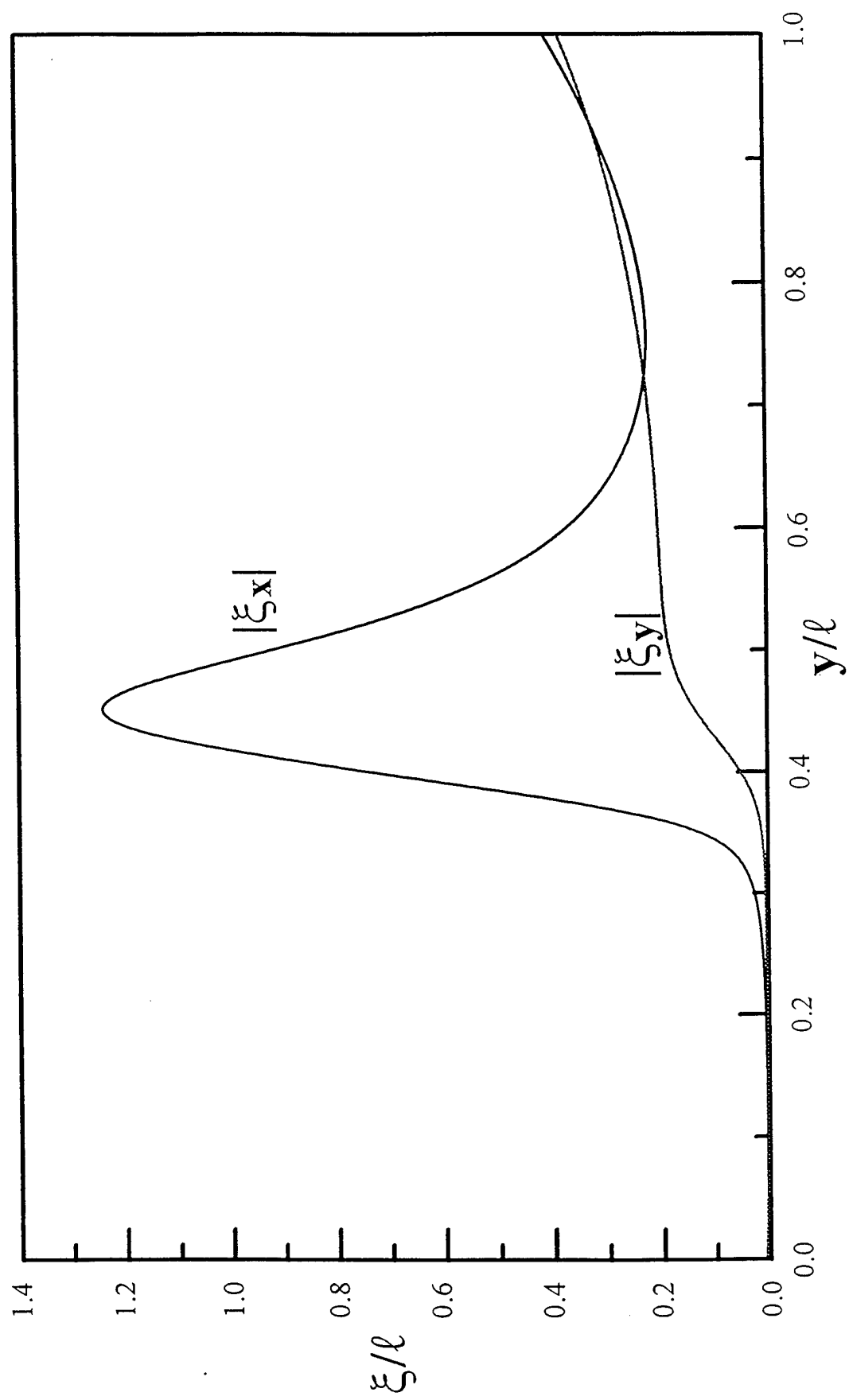


Fig. 11

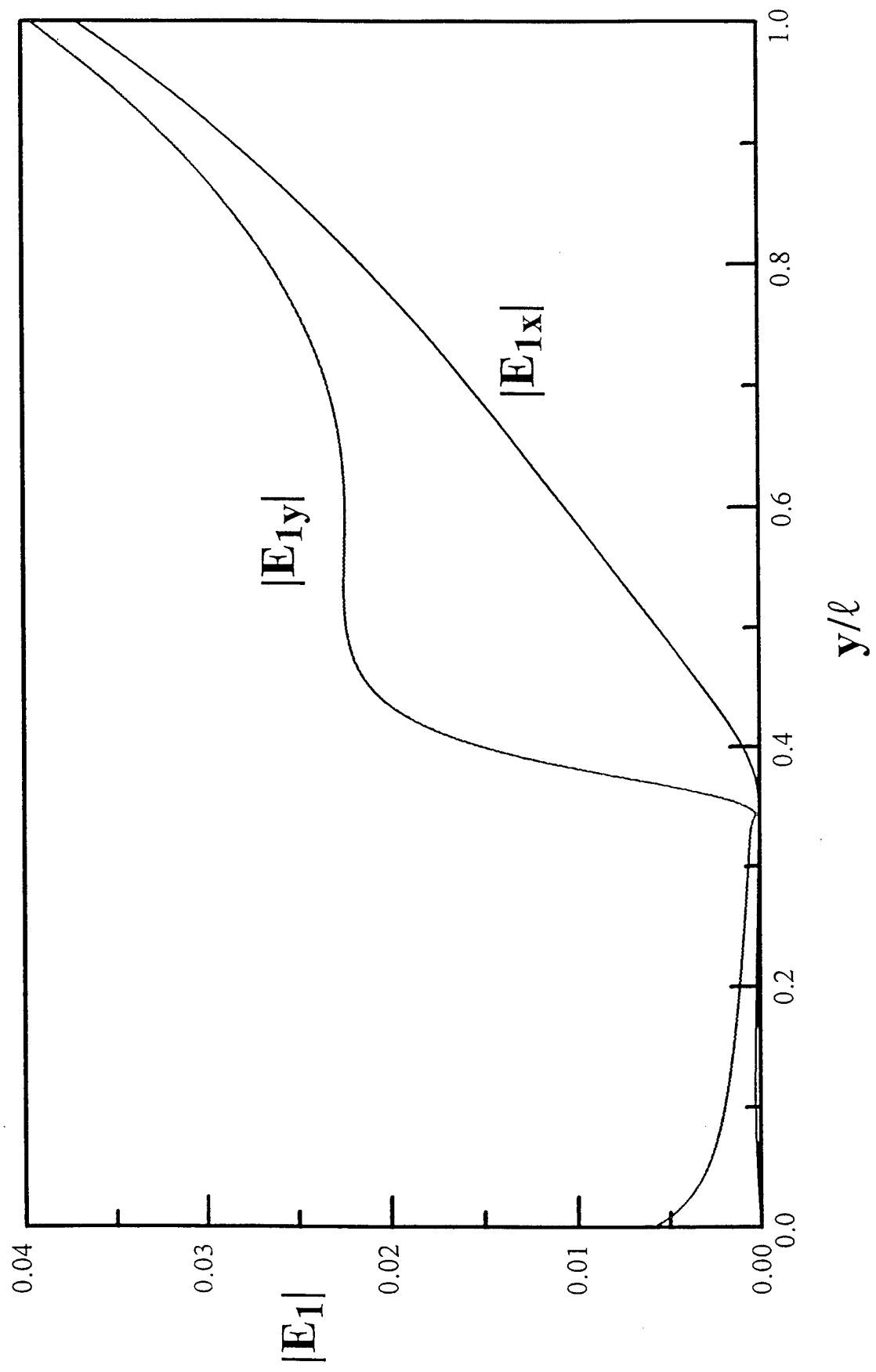


Fig. 12

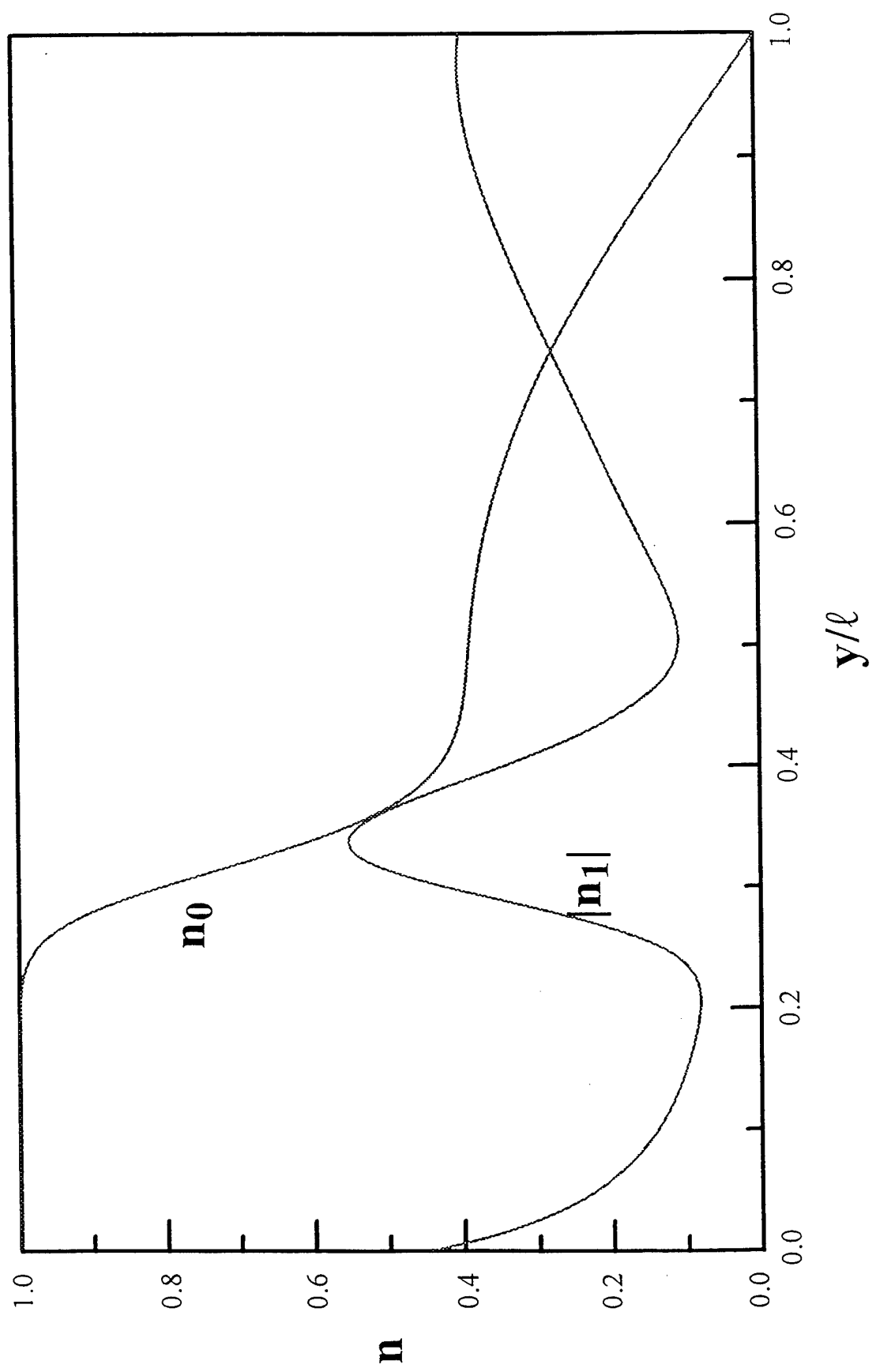


Fig. 13

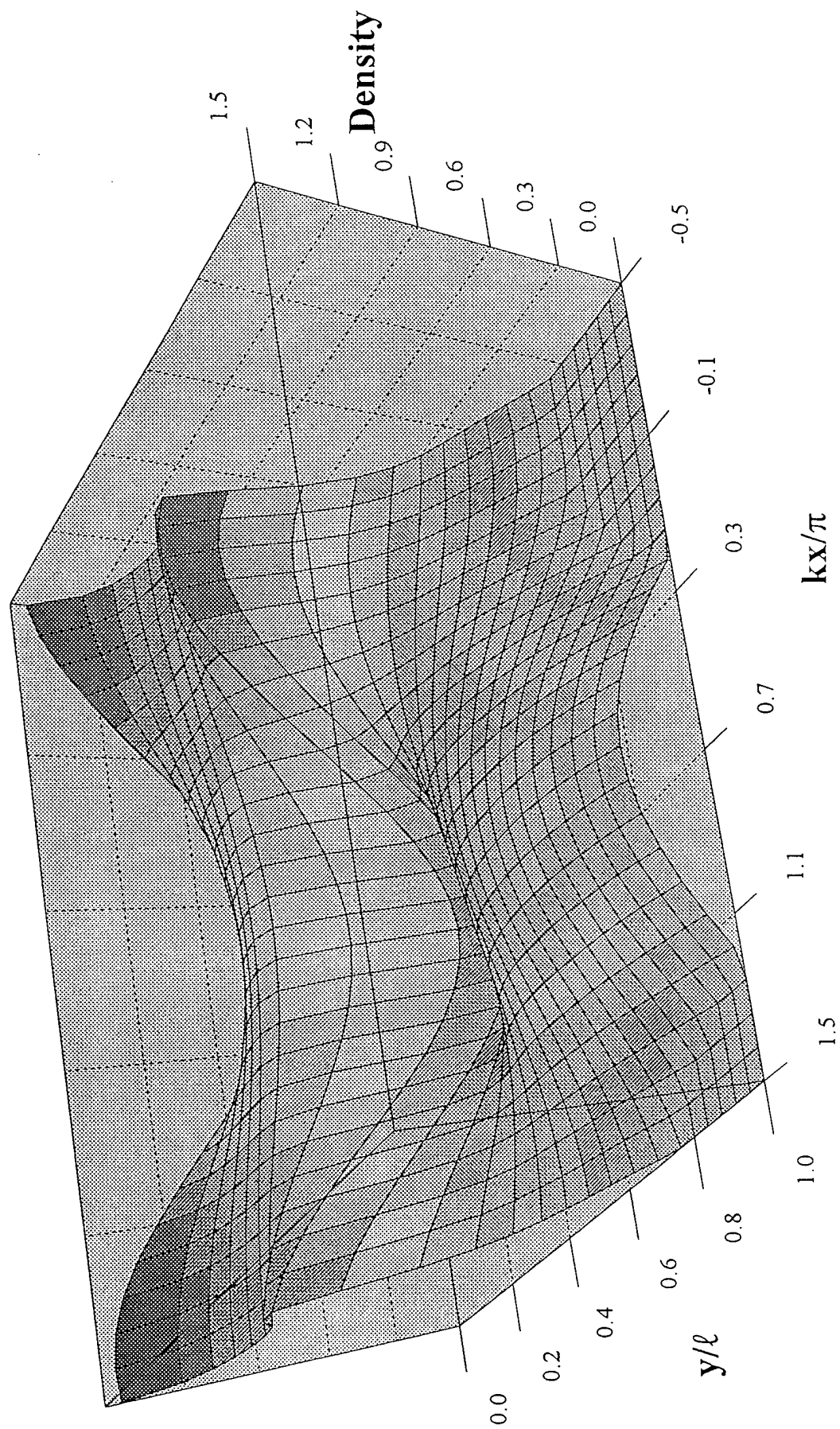


Fig.14

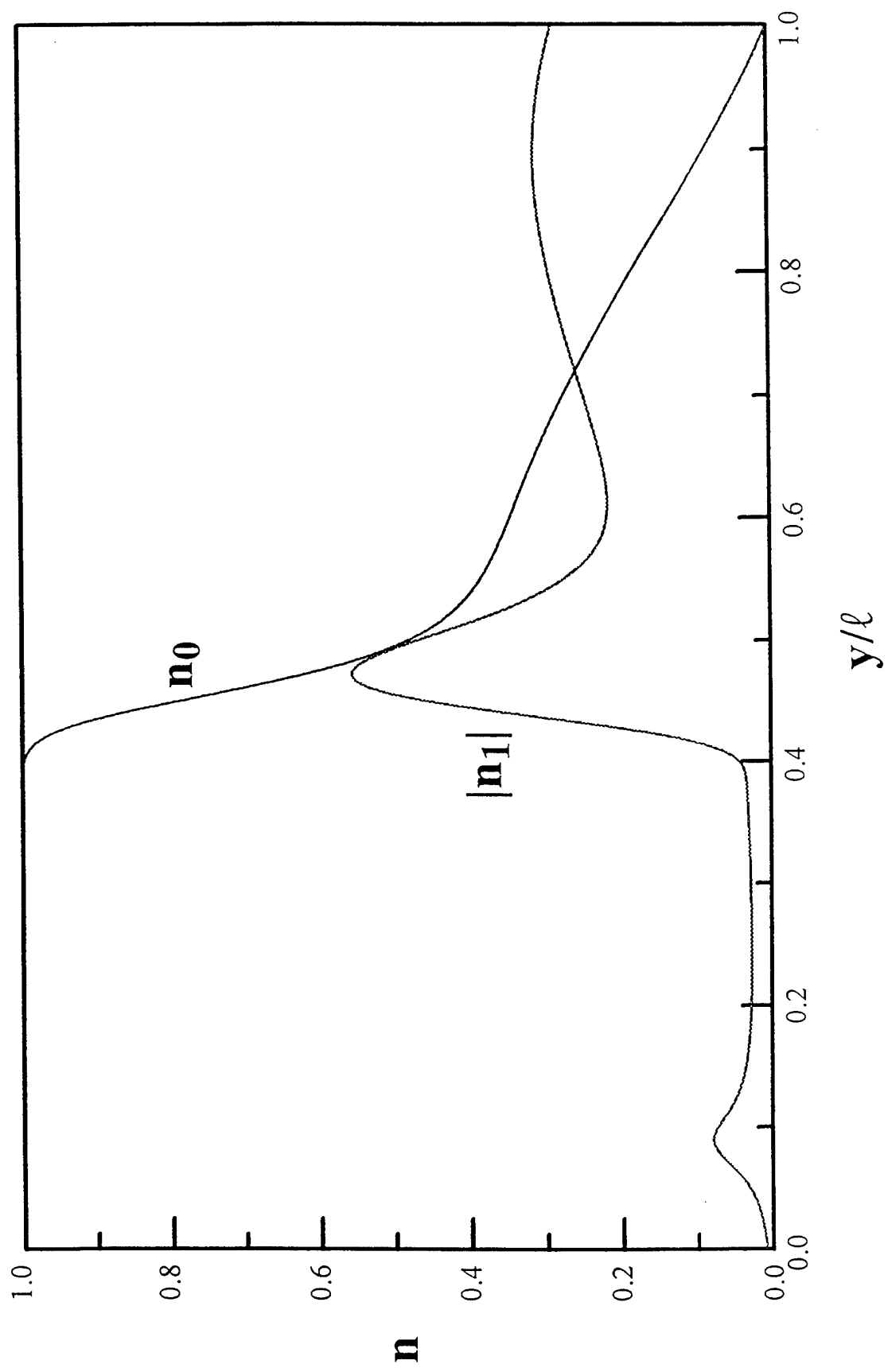


Fig. 15

